PHYSOR 2014 - The Role of Reactor Physics toward a Sustainable Future
The Westin Miyako, Kyoto, Japan, September 28 - October 3, 2014, on CD-ROM (2014)

A LOW ORDER NONLINEAR TRANSPORT ACCELERATION SCHEME FOR THE METHOD OF CHARACTERISTICS

Lulu Li, Kord Smith, and Benoit Forget
Department of Nuclear Science & Engineering
Massachusetts Institute of Technology, Cambridge, MA 02139 USA
lululi@mit.edu
kord@mit.edu
bforget@mit.edu

Rodolfo Ferrer
Studsvik Scandpower, Inc.
1070 Riverwalk Drive, Suite 150
Idaho Falls, ID 83402 USA
rodolfo.ferrer@studsvik.com

ABSTRACT

This study presents a new physics-based multi-grid nonlinear acceleration method, henceforth referred to as the Low-Order Operator (LOO) method, which uses a coarse space-angle multi-group Method of Characteristics (MOC) neutron transport calculation to accelerate the fine space-angle MOC calculation. LOO is designed to capture more angular effects than diffusion-based acceleration methods through a transport-based low-order solver. LOO differs from the two existing transport-based acceleration schemes in that it emphasizes simplified coarse space-angle characteristics and preserves physics in quadrant phase-space. The details of the method, including the restriction step, the low-order iterative solver, and the prolongation step are discussed in this work. The performance of LOO is compared to the Coarse-Mesh Finite Difference method (CMFD) in benchmark problems. LOO shows comparable convergence compared to CMFD, and does not require under-relaxation to converge, making it a robust acceleration scheme.

Key Words: **Neutron transport theory, methods of characteristics (MOC), acceleration, low order transport, multi-grid.**

1. INTRODUCTION

The Methods of Characteristics (MOC) is a widely used technique for solving partial differential equations in reactor physics applications. Examples include codes such as the CACTUS module in WIMS[1], DRAGON[2], CASMO [3], CHAPLET[4], CRX[5], APOLLO2[6], DeCART[7], MCCA3D[8] and MPACT[9]. While MOC is an attractive method to solve the neutron transport equation, it requires many iterative transport sweeps to resolve large heterogeneous LWR problems. In order to make MOC practical to implement, various acceleration schemes have been

developed to reduce the number of transport sweeps necessary to achieve convergence as defined by a convergence criteria.

Various diffusion-based acceleration methods have been developed that approximate the scalar flux correction to the high-order scalar flux. The most widely one is the Coarse-Mesh Finite Difference method (CMFD). Ref. [10] provides a summary of various diffusion-based acceleration methods and describes CMFD's dependency on under-relaxation or damping factor to converge certain problems. For instance, the C5G7 benchmark problem[11] is an example of a problem in which CMFD has difficulty converging without under-relaxation.

Limited work has been performed using a low-order transport method. Two examples of such works are Smith and Rhodes' "micro-tracks" method [12] and Grassi's non-linear space-angle multi-grid acceleration method[13]. The former lays down macro-tracks directly on top of the micro-tracks of the fine-grid MOC, and the latter is based on a very general coarse angle-space discretization. Both methods tend to require more high-order transport sweeps than CMFD except when CMFD has difficulty converging.

Wolters and Larsen proposed two generalized Monte Carlo-CMFD methods. By using angular moments of the transport equation these methods "were consistently more accurate, and had less variance" than the traditional CMFD method[14]. Though no one has successfully demonstrated these methods in more than one dimension. LOO uses angular flux moments, and is implemented in two dimensions, easily extendable to three dimensions. It is currently implemented to accelerate a deterministic transport method.

2. METHODOLOGY

2.1. LOO Overview

LOO defines a simple set of coarse-grid characteristics, where eight tracks are laid down in each coarse-mesh cell connecting the centers of neighboring surfaces. For instance, Fig. 1 displays low-order tracks in 3x3 square acceleration cells. The center cell is further illustrated with 4 forward low-order tracks and 4 backward low-order tracks. Physically, the forward and backward pair of tracks occupy the same quadrant angle-space.

The implementation in this study defines a unique source for each of the eight tracks in the coarse-mesh cell, and they are assumed to share the same coarse-mesh cell homogenized cross sections. LOO iteratively solves the low-order system using MOC transport sweeps. By conserving the first-order spatial and angular moments, LOO is designed to capture more angular effects than CMFD. Fig. 2 provides a flow chart of the overall algorithm.

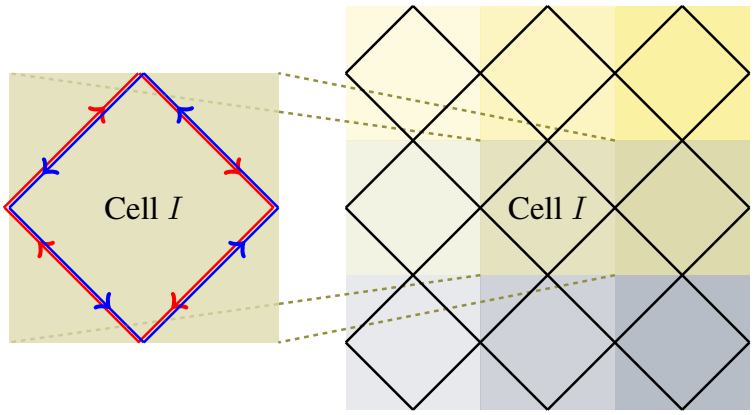

Figure 1. Illustration of Coarse Mesh Characteristics In Cell I

2.2. Notation

This study uses the following subscripts:

g = energy group index	s = surface index
a = azimuthal angle index	p = polar angle index
m = solid angle index, combining a, p	k = segment index
i = flat source region (FSR) index	I = coarse-mesh acceleration cell index
q = surface's quadrant index	t = cell's low-order track index, ranging from 1 to 8

Overhead bars (i.e., $\overline{x}$) designate coarse-mesh homogenized quantities, and hats (i.e., $\hat{x}$) designate quadrant-integrated quantities. This study uses the following quadrant-integrated terms:

$$\hat{J} = \text{surface-averaged quadrant-integrated currents (quadrant currents)}$$
$$\hat{\psi} = \text{quadrant-integrated angular fluxes (quadrant fluxes)}$$
$$\hat{q} = \text{quadrant-integrated sources (quadrant sources)}$$

There are four quadrant currents associated with each surface. For instance Fig. 3 illustrates the four quadrant currents on surface s of coarse mesh cell I (painted in blue). The sum of the two quadrant currents pointing towards the same side of the surface equals the partial current. The sum of all four quadrant currents yields the net current on that surface.

Additionally, there are two parenthesized superscripts referring to iteration indexes:

$$^{(h)} = \text{high-order MOC sweep} \qquad ^{(l)} = \text{low-order MOC sweep}$$

In particular, the half superscript $^{(h+1/2)}$ refers to results of the h-th high-order MOC sweep. For instance, the h-th high-order MOC sweep generates FSR scalar fluxes $\overline{\phi}_{g,i}^{(h+1/2)}$. Then a low-order MOC problem is solved, and the converged low-order solution is designated with $^{(l=\infty)}$. Prolongation using the converged low-order solution produces the FSR scalar fluxes to be used in the next high-order MOC sweep.

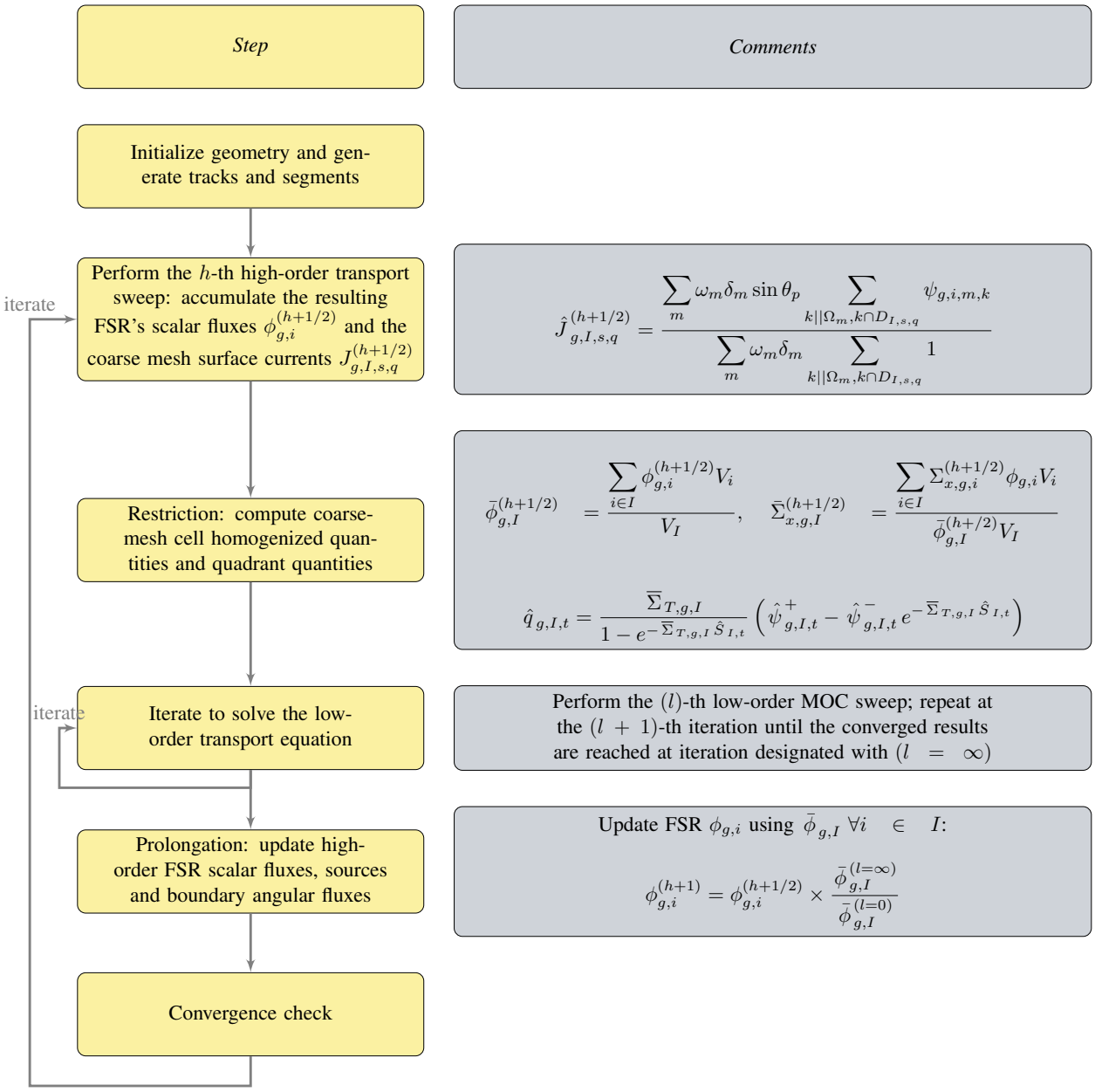

Figure 2. LOO Flow

2.3. Tallying of Quadrant Currents

During a fine-grid MOC sweep, the quadrant currents are tallied using Eq. 1. The quadrant currents are accumulated from the angular fluxes $\psi_{g,i,m,k}$ whose 2D projections intersect the I-th coarse-

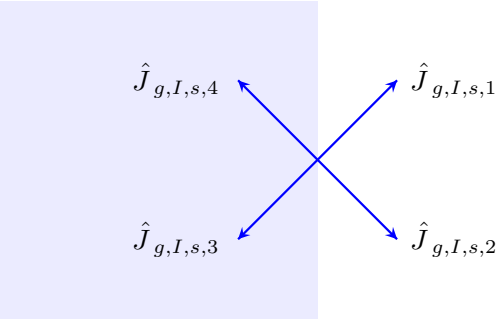

Figure 3. Illustration of Quadrant Current $\hat{J}_{g,I}^{s,q}$

mesh cell's s-th surface in the q-th quadrant.

$$\hat{J}_{g,I,s,q}^{(h+1/2)} = \frac{\sum_m \omega_m \delta_m \sin\theta_p \sum_{k||\Omega_m, k\cap D_{I,s,q}} \psi_{g,i,m,k}}{\sum_m \omega_m \delta_m \sum_{k||\Omega_m, k\cap D_{I,s,q}} 1} \tag{1}$$

Currently this study has only implemented square coarse-mesh cells for simplicity, though extending the algorithm to rectangular coarse-mesh cells is expected to be relatively straightforward.

By superimposing the acceleration mesh on the fine-grid MOC representation, often times a number of high-order MOC tracks go through the corners of the coarse-mesh cells. The treatment of these tracks should not be neglected and is discussed in Appendix A.

2.4. Restriction

The coarse-mesh volume-averaged scalar fluxes and the flux-weighted cross sections are calculated in the same manner as traditional CMFD methods:

$$\overline{\phi}_{g,I}^{(h+1/2)} = \frac{\sum_{i\in I} \phi_{g,i}^{(h+1/2)} V_i}{V_I}, \qquad \overline{\Sigma}_{g,x,I}^{(h+1/2)} = \frac{\sum_{i\in I} \Sigma_{g,x,i}^{(h+1/2)} \phi_{g,i} V_i}{\overline{\phi}_{g,I}^{(h+/2)} V_I} \tag{2}$$

The quantities of interest during the low-order MOC sweep are the quadrant fluxes. Quadrant fluxes can be calculated from the quadrant currents as follows:

$$\hat{\psi}_{g,I,s,q}^{(h+1/2)} = \frac{\hat{J}_{g,I,s,q}^{(h+1/2)}}{\cos\left(\frac{\pi}{4}\right) \cdot \sin\theta_{p0}} \tag{3}$$

where the cosine term arises from the fact that the quadrant flux represents the characteristic track in direction $\frac{\pi}{4}$ from the surface's normal direction. For simplicity, the low-order system uses one polar angle θ_{p0} taken from the Tabuchi-Yamamoto quadrature set [15] [1], while the high-order

[1] One could use more polar angles.

system tends to use three polar angles. Recall that $\hat{J}_{g,I,s,q}$ includes the 2D projections of all polar angles from a high-order sweep. Dividing by $\sin\theta_{p0}$ preserves the equivalence in 3D, allowing LOO to perform low-order sweeps using one polar angle.

Up to this point, the $\hat{\psi}_{g,I,s,q}$ notation (defined in Eq. 3) has been used to identify quadrant fluxes based on the mesh surfaces they were tallied on. Moving forward, it is easier to use the notation $\hat{\psi}^{\pm}_{g,I,t}$, which identifies quadrant fluxes as the incoming (-) or outgoing (+) angular flux of low-order track t (ranging from 1 to 8) inside of coarse-mesh I.

Also the superscript $^{(h+1/2)}$ is dropped in the rest of this subsection because all variables in the restriction step are results from the (h)-th high-order MOC sweep.

Another quantity of interest is the t-th low-order characteristic source in coarse-mesh cell I:

$$\hat{q}_{g,I,t} = \frac{\overline{\Sigma}_{T,g,I}}{1 - e^{-\overline{\Sigma}_{T,g,I}\hat{S}_{I,t}}} \left(\hat{\psi}^{+}_{g,I,t} - \hat{\psi}^{-}_{g,I,t} e^{-\overline{\Sigma}_{T,g,I}\hat{S}_{I,t}} \right) \tag{4}$$

Eq. 4 is derived from Eq. 5, the solution of MOC equation, to explicitly preserve the MOC angular flux for the t-th low-order track within the I-th coarse-mesh cell, given the assumption of a spatially invariant coarse-mesh cell cross section $\overline{\Sigma}_{T,g,I}$:

$$\hat{\psi}^{+}_{g,I,t} = \hat{\psi}^{-}_{g,I,t} e^{-\overline{\Sigma}_{T,g,I}\hat{S}_{I,t}} + \frac{\hat{q}_{g,I,t}}{\overline{\Sigma}_{T,g,I}} \left(1 - e^{-\overline{\Sigma}_{T,g,I}\hat{S}_{I,t}} \right) \tag{5}$$

In summary, three key steps have been described in this section: the generation of the low-order tracks, the tallying of the incoming angular fluxes, and the definition of the low-order tracks' source and cross sections.

2.5. Solving the Low-Order Problem

LOO accelerates the fission source iteration by solving the two-dimensional, multi-group, single polar angle low-order MOC problem in the same iterative manner as in standard MOC. A brief description of the solution scheme is given below:

1. Initialize the first low-order MOC sweep $(l = 0)$ with results from the last high-order MOC sweep:

$$\overline{\phi}^{\,(l=0)}_{g,I} = \overline{\phi}^{\,(h+1/2)}_{g,I} \qquad k_{\text{eff}}{}^{(l=0)} = k_{\text{eff}}{}^{(h+1/2)} \tag{6}$$

2. Compute the coarse-mesh averaged sources:

$$\overline{q}^{\,(l)}_{g,I} = \frac{1}{4\pi} \sum_{g'} \left[\overline{\Sigma}^{(h+1/2)}_{s,g'\to g,I} + \frac{\chi^{(h+1/2)}_{g,I}}{k_{\text{eff}}{}^{(l)}} \overline{\nu\Sigma}^{(h+1/2)}_{f,g',I} \right] \overline{\phi}^{\,(l)}_{g',I} \tag{7}$$

3. Compute the quadrant sources:

$$\hat{q}_{g,I,t}^{(l)} = \hat{q}_{g,I,t}^{(h+1/2)} \frac{\overline{q}_{g,I}^{(l)}}{\overline{q}_{g,I}^{(h)}} \tag{8}$$

where $\overline{q}_{g,I}^{(h)}$ is the coarse-mesh homogenized source used to perform the (h)-th high-order MOC sweep. This equation performs a multiplicative update using the most recent mesh-cell homogenized source to compute the new quadrant source.

4. Perform a low-order MOC iteration sweeping through the coarse characteristic tracks. The outgoing angular flux $\hat{\psi}_{g,I,t}^{+}$ of each track is computed from $\hat{\psi}_{g,I,t}^{-}$, $\overline{\Sigma}_{T,g,I}$, $\hat{S}_{I,t}$ and $\hat{q}_{g,I,t}$ using Eq. 5.

5. Compute the coarse-mesh averaged scalar flux $\overline{\phi}_{g,I}^{(l+1)}$. Two implementations are investigated in this study:

   (a) LOO-1 method, where the summation of the tracks' averaged angular fluxes (Eq. 9) is used as a multiplicative update for the coarse-mesh's scalar flux as in Eq. 10:

$$\sum_{t=1}^{8} \overline{\hat{\psi}}_{g,I,t}^{(l+1)} = \sum_{t=1}^{8} \left(\frac{\hat{q}_{g,I,t}^{(l)}}{\overline{\Sigma}_{T,g,I}^{(h+1/2)}} + \frac{\hat{\psi}_{g,I,t}^{-,(l)} - \hat{\psi}_{g,I,t}^{+,(l)}}{\overline{\Sigma}_{T,g,I}^{(h+1/2)} \hat{S}_{I,t}} \right) \tag{9}$$

$$\overline{\phi}_{g,I}^{(l+1)} = \overline{\phi}_{g,I}^{(h+1/2)} \frac{\sum_{t=1}^{8} \overline{\hat{\psi}}_{g,I,t}^{(l+1)}}{\sum_{t=1}^{8} \overline{\hat{\psi}}_{g,I,t}^{(h+1/2)}} \tag{10}$$

   (b) LOO-2 method, where the scalar fluxes are solved from the neutron balance equation. The net leakage of each coarse-mesh is tallied:

$$L_{g,I}^{(l+1)} = \hat{\omega}\ \hat{\delta} \sin\theta_p \sum_{t,\pm} \left(\pm\, \hat{\psi}_{g,I,t}^{\pm,(l+1)} \right) = \hat{\omega}\ \hat{\delta} \sin\theta_p \sum_{t=1}^{8} \left(\hat{\psi}_{g,I,t}^{+,(l+1)} - \hat{\psi}_{g,I,t}^{-,(l+1)} \right) \tag{11}$$

where $\hat{\omega}$, $\hat{\delta}$ are identical among all low-order characteristic tracks because they are symmetric and occupy equivalent angle-space phase space.
Then by re-writing the neutron balance equation for coarse-mesh I,

$$L_{g,I}^{(l+1)} + \overline{\Sigma}_{T,g,I}^{(h+1/2)}\ \overline{\phi}_{g,I}^{(l+1)}\, V_I = 4\pi\ \overline{q}_{g,I}^{(l+1)}\, V_I \tag{12}$$

the updated coarse-mesh scalar flux can be calculated,

$$\overline{\phi}_{g,I}^{(l+1)} = \frac{4\pi\ \overline{q}_{g,I}^{(l+1)}\, V_I - L_{g,I}^{(l+1)}}{\overline{\Sigma}_{T,g,I}^{(h+1/2)}\, V_I} \tag{13}$$

6. Calculate the new low-order eigenvalue ${k_{\text{eff}}}^{(l+1)}$:

$$ {k_{\text{eff}}}^{(l+1)} = \frac{\sum_I V_I \sum_g \overline{\nu\Sigma}_{f,g,I}^{(h+1/2)} \ \overline{\phi}_{g,I}^{(l+1)}}{\sum_I \sum_g L_{g,I}^{(l+1)} + \sum_I V_I \sum_g \overline{\Sigma}_{a,g,I}^{(h+1/2)} \ \overline{\phi}_{g,I}^{(l+1)}} \tag{14} $$

where $\sum_I \sum_g L_{g,I}^{(l+1)}$ is the total leakage term. Alternatively, the global leakage term can be computed by summing the net current leaving the geometry's outer boundaries.

7. Compute the L2 norm of successive iteration relative change in energy-integrated coarse-mesh fission source,

$$ \epsilon^{(l+1)} = \sqrt{\frac{1}{N_I} \sum_I \left(\frac{\sum_g \overline{\nu\Sigma}_{f,g,I} \phi_{g,I}^{(l+1)} - \sum_g \overline{\nu\Sigma}_{f,g,I} \phi_{g,I}^{(l)}}{\sum_g \overline{\nu\Sigma}_{f,g,I} \phi_{g,I}^{(l)}} \right)^2} \tag{15} $$

where N_I is the total number of coarse mesh cells.

The previous steps are repeated from step 2 until $\epsilon^{(l+1)}$ meets the low-order convergence criteria. The converged cell-averaged scalar flux is defined as $\overline{\phi}_{g,I}^{(\infty)}$ where the superscript (∞) designates that it is the converged result.

2.6. Prolongation

The FSR scalar flux prolongation is the same as in CMFD, where the FSR scalar fluxes computed from the high-order transport sweep is multiplied by the ratio of the cell-averaged scalar flux before and after the LOO steps. Each fine-grid boundary angular flux is updated by the quadrant flux it belongs to, i.e.,

$$ \phi_{g,I}^{(h+1)} = \phi_{g,I}^{(h+1/2)} \frac{\overline{\phi}_{g,I}^{(l=\infty)}}{\overline{\phi}_{g,I}^{(h+1/2)}} \qquad \psi_{B,g,m}^{(h+1)} = \psi_{B,g,m}^{(h+1/2)} \frac{\hat{\psi}_{g,I,t}^{-,(l=\infty)}}{\hat{\psi}_{g,I,t}^{-,(h+1/2)}} \tag{16} $$

where the boundary flux $\psi_{B,g,m}$ exits the geometry along coarse-mesh I's track t with the "$-$" subscript designate an outgoing angular flux.

3. RESULTS

This study implemented CMFD, LOO-1 and LOO-2 in OpenMOC, an open-source two-dimensional MOC code developed at MIT for solving heterogeneous reactor problems. The accuracy and performance of OpenMOC's high-order MOC solver can be found in Ref. [16]. In each of the following test cases the three acceleration methods share the identical high-order MOC representation and the same coarse-mesh cells. In all three methods, the low-order systems are iteratively solved until the L2 norm of the relative change in successive fission sources is below 1e-6.

3.1. C5G7 Benchmark Problem

The 2D C5G7 benchmark problem [11] contains two MOX and two UO_2 fuel assemblies surrounded by water. Each fuel assembly contains 17x17 pin cells, including guide tubes and a central fission chamber. Each lattice has a 1.26 cm pin pitch with a 0.54 cm pin radius. The physical geometry is displayed in the left side of Fig. 4.

The high-order MOC uses 7 energy groups, 0.05 cm track spacing, 64 azimuthal angles and 3 polar angles. All acceleration methods use pin-level coarse meshes and 7 energy groups.

As shown in Fig. 5, for this problem CMFD method needs a DF less than 0.9 to converge, and the optimal DF is approximately 0.6 to 0.7. Fig. 4 compares the convergence of CMFD (with the optimal DF) and the two LOO methods without DFs. The three methods converge very similarly for this problem.

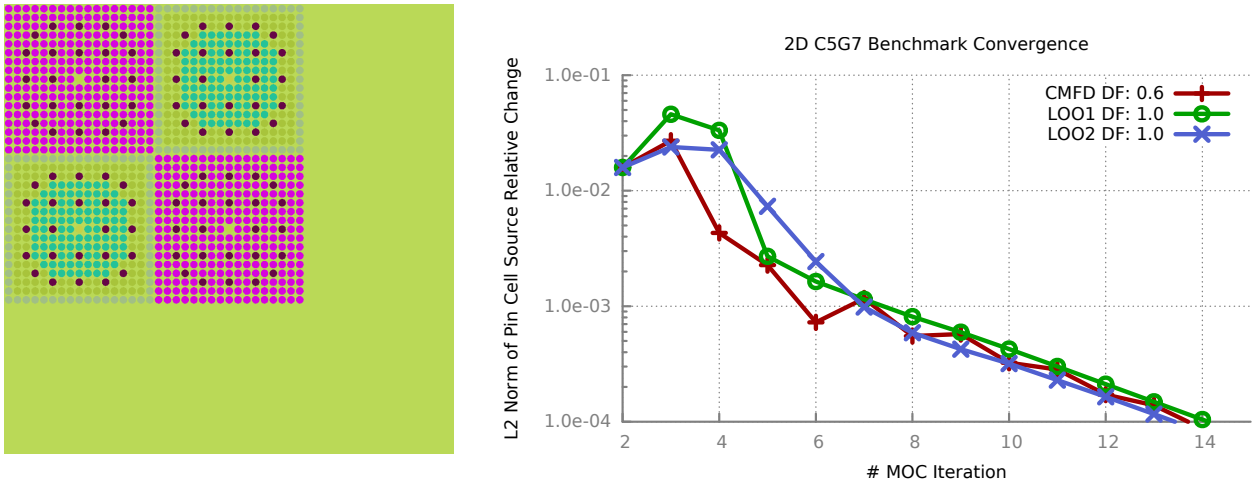

Figure 4. 2D C5G7 Benchmark Problem Results

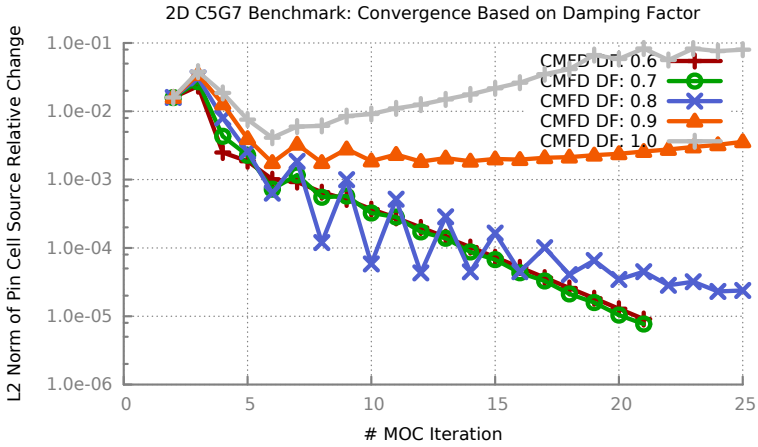

Figure 5. Impact of DFs on CMFD Convergence in the 2D C5G7 Benchmark Problem

3.2. Quarter Core Problem

This problem represents a quarter-core pseudo PWR with two reflective and two vacuum boundary conditions. It consists of 10 UO_2 and 12 MOX assemblies surrounded by water. The fuel assemblies' composition and cross-sections are taken from the C5G7 benchmark problem.

The high-order MOC discretization has a 0.05 cm track spacing and 32 azimuthal angles, generating 52,460 tracks and 30,969,602 segments[2]. The low-order MOC employs 10,404 pin-level coarse-mesh cells. As shown in Fig. 6, the convergence behaviors of the three methods are very similar.

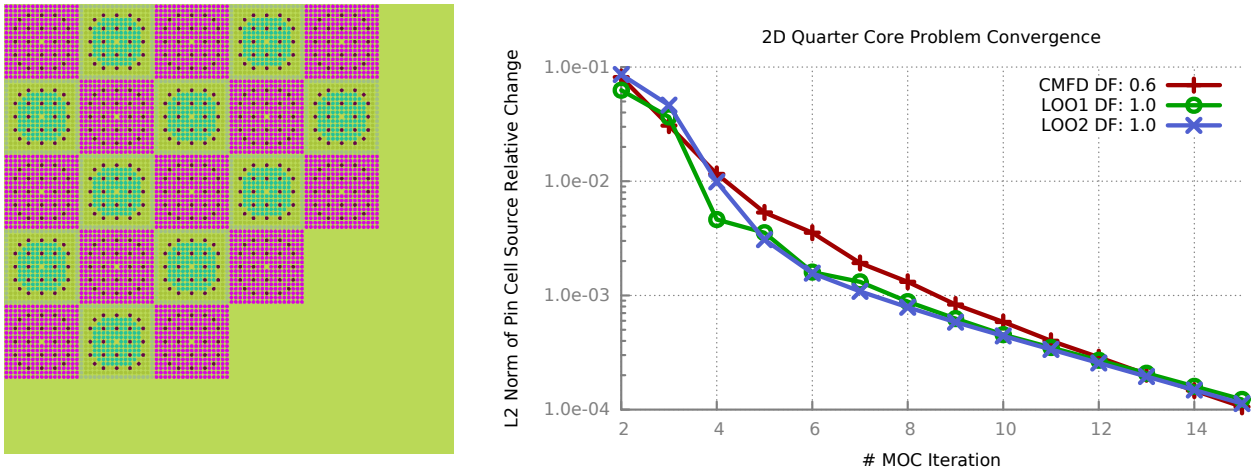

Figure 6. 2D Quarter Core Problem Results

3.3. B&W Critical Assemblies

This section models cores from the Babcock & Wilcox (B&W) 1484 and 1810 Series [17, 18]. For example, core 1 of the 1810 series consists of a 5x5 array of 15x15 PWR assemblies with a 1.64 cm pitch and a 2.46 wt% uniform fuel enrichment. These cores contain different amount of boron concentration and some contain gadolinium fuel pins or Ag-In-Cd (AIC), B_4C control rods or hollow rods depending on the problem.

CASMO-4E calculations [19] were performed to generate eight group cross sections. For simplicity, OpenMOC uses a representative cross-section for each material type. The high-order MOC representation uses 0.05 cm track spacing, 64 azimuthal angles and 3 polar angles. For these cores, CMFD's optimal damping factor based on trial and error is approximately 0.5 and it is used to generate the results below.

Fig. 7 shows the number of high-order transport sweeps needed for each of the three methods to converge to a 1e-4 L2 norm of the relative change in pin cell fission source. The three methods' convergence behaviors are very similar for the B&W critical series.

[2] A track refers to a high-order MOC track that goes from one external boundary to another. A segment refers to a portion of the track that is contained in a single FSR.

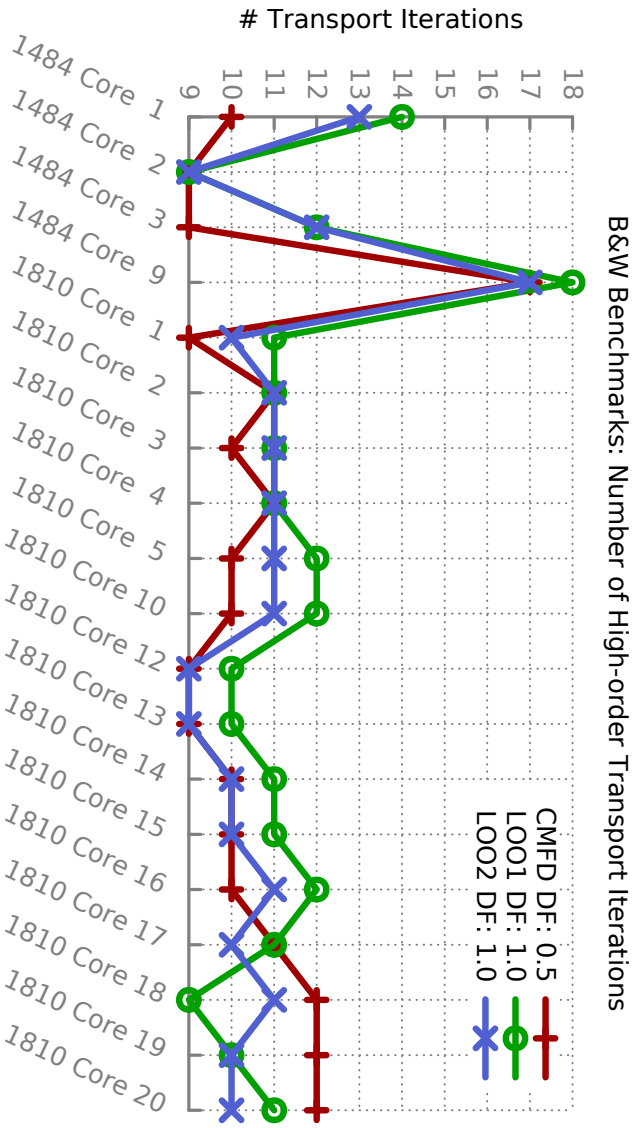

Figure 7. B&W Critical Cores Results

4. CONCLUSIONS

This work demonstrates the performance of LOO, a low-order transport acceleration scheme for accelerating the high-order transport equation. LOO addresses the challenges of slow convergence in solving large heterogeneous reactor problems. LOO employs a low-order transport solver to conserve the first-order spatial and angular moments. While CMFD accounts for the self-scattering source by defining a group removal cross-section, LOO treats the self-scattering term as part of the group-to-group scattering source because of the transport operator's dependence on angular flux.

Based on the 2D PWR test cases performed in this work, LOO requires similar number of high-order transport sweeps compared to CMFD. In addition, CMFD acceleration routinely requires damping factors to converge large problems, while LOO does not need under-relaxation in any problem tested in this work.

In this work LOO is shown to be robust and effective in accelerating 2D MOC solutions using a single level acceleration mesh. It is straight-forward to extend LOO into a multi-level scheme similar to multi-level CMFD.

5. ONGOING WORK

Investigations are underway to evaluate other closure relationships for the LOO system. One example is where different cross sections are employed for each quadrant source computation. To date, no effort has be expended to minimize the computational efforts required to solve the LOO equations. When optimal LOO closure relationships have been fully determined, efficiency in the solution of the LOO equations will be addressed.

The primary goal of this work has been to explore low-order transport acceleration for deterministic transport methods in preparation for applications to accelerate Monte Carlo fission source convergence. The goal is to have LOO closure relationships that are less sensitive to statistical fluctuations than traditional CMFD methods which rely on acceleration boundary net currents.

ACKNOWLEDGMENTS

The first author would like to acknowledge Studsvik Scandpower for providing fellowship support for this study.

REFERENCES

[1] M. J. Halsall. *CACTUS, A Characteristics Solution to the Neutron Transport Equations in Complicated Geometries*. *Technical report*, United Kingdom Atomic Energy Authority (1980).

[2] G. Marleau, R. Roy, and A. Hebert. *DRAGON: A Collision Probability Transport Code for Cell and Supercell Calculations*. Institut de genie nuclearire, Ecole Polytechnique de Montreal. IGE-157 (1994).

[3] D. Knott, B. H. Forssen, and M. Edenius. *CASMO-4 Methodology Manual*. Sutdsvik of America. SOA-95/02 (1995).

[4] S. Kosaka *et al.* "The characteristics transport calculation for a multi-assembly system using neutron path linking technique." *Proceedings of International Conference on Mathematics Compatations Reactor Physics and Environmental Analysis of Nuclear System* (1999).

[5] N. Z. Cho *et al.* "Whole-core heterogeneous transport calculations and their comparisons with diffusion results." *Trans. Am. Nucl. Soc.*, **83(292)** (2000).

[6] R. Sanchez, I. Zmijarevic *et al.* "Apollo2 year 2010." *Journal of Nuclear Engineering and Technology*, **42(5)**: pp. 474–499 (2010).

[7] H. G. Joo *et al.* "Methods and performance of a three-dimensional whole-core transport code de-cart." In: *Proc. PHYSOR*. Chicago, IL, USA (2004).

[8] I. R. Suslov *et al.* "Method of characteristics for calculation of vver without homogenization." In: *Proceedings of International Conference on Mathematics and Computational Methods Applied to Nuclear Science and Engineering (M&C 2005)*. American Nuclear Society, Avignon, France (2005).

[9] B. Kochunas. *A Hybrid Parallel Algorithm for the 3-D Method of Characteristics Solution of the Boltzmann Transport Equation on High Performance Computer Clusters*. Phd dissertation, University of Michigan, Nuclear Engineering and Radiological Sciences (2013).

[10] Lulu Li. "A Low Order Acceleration Scheme for Solving the Neutron Transport Equation." M.S. Thesis, Massachusetts Institute of Technology. URL http://hdl.handle.net/1721.1/86422 (2013).

[11] M. A. Smith, E. E. Lewis, and B.-C. Na. *Benchmark on Deterministic Transport Calculations Without Spatial Homogenisation: A 2-D/3-D MOX Fuel Assembly Benchmark. Technical report*, Nuclear Energy Agency Organisation for Economic Co-Operation and Development (2003).

[12] K. S. Smith and J. D. Rhodes. "Casmo characteristics method for two-dimentional pwr and bwr core calculations." *Trans. Am. Nucl. Soc.* (2000).

[13] G. Grassi. "A nonlinear space-angle multigrid acceleration for the method of characteristics in unstructured meshes." *Nucl. Sci. Eng.*, **155**: pp. 208–222 (2007).

[14] E. R. Wolters, E. W. Larsen, and W. R. Martin. "Generalized hybrid monte carlo-cmfd methods for fission source convergence." In: *Proceedings of International Conference on Mathematics and Computational Methods Applied to Nuclear Science and Engineering (M&C 2011)*. American Nuclear Society, Rio de Janeiro, RJ, Brazil (2011).

[15] A. Yamamoto *et al.* "Derivation of optimum polar angle quadrature set for the method of characteristics based on approximation error for the bickley function." *Journal of Nuclear Science and Engineering*, **44(2)**: pp. 129–136 (2007).

[16] W. Boyd *et al.* "The openmoc method of characteristics neutral particle transport code." *Annals of Nuclear Energy*, **68**: pp. 43–52 (2014).

[17] M. N. Baldwin *et al. Critical Experiments Supporting Close Proximity Water Storage of Power Reactor Fuel. Technical report*, Babcock & Wilcox (1979).

[18] L. W. Lewman. *Urania-Gadolinia: Nuclear Model Development and Critical Experiment Benchmark. Technical Report B&W 1810, DOE/ET/34212-41*, Babcock & Wilcox (1984).

[19] Sutdsvik Scandpower, Inc. *CASMO-4E User's Manual*. SSP-09/442-U Rev 0 (2009).

APPENDIX A. Treatment of Corner Tracks

One aspect that is easy to overlook is the high-order MOC tracks that intersect the corners of coarse-mesh cells. These tracks need to be accounted for correctly to preserve neutron balance. One solution is to physically move these corner tracks a small distance from the corners. This study chooses to keep the corner tracks' positions, tally the quantities on the corners, and split the tallied results equally among neighboring surfaces.

For instance, a corner track is between Cell IV and Cell II as illustrated in blue in Fig. 8. The corner track treatment mimics the effect of replacing the physical track (solid blue line) with two virtual tracks (red and green dashed lines) each with half of the tallied value. Both the forward (left plot) and backward (right plot) directions need to be treated consistently. Taking the forward direction (left plot) as an example, half of the tallied result is added on the top surface of Cell IV and the left surface of Cell I (red dashed line), the left surface of Cell IV and top surface of Cell III (green dashed line).

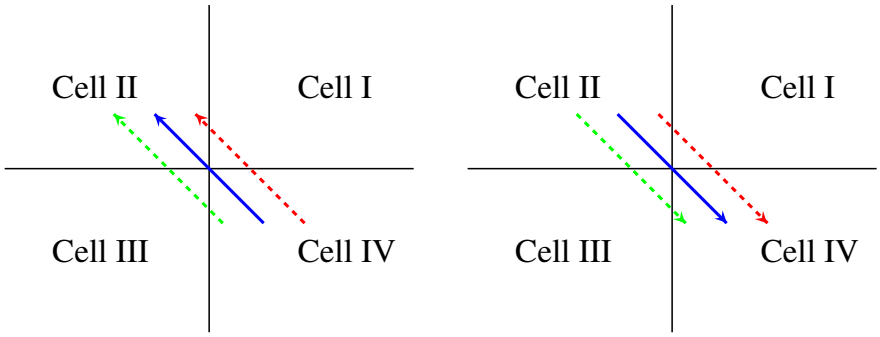

Figure 8. Illustration of Corner Splitting Method For Interior Cells

One special case is the corner tracks intersecting the reflective geometry boundaries. As in Fig. 9, in the forward direction (left plot), the red dashed virtual track only needs to be tallied on the top surface of Cell II, and it does not have any impact on the left surface of Cell I because of the reflective boundary condition. The green dashed virtual track is reflected from the left surface of Cell II, and needs to be tallied on the top surface of Cell II in a quadrant angle-space that differs from its original track.

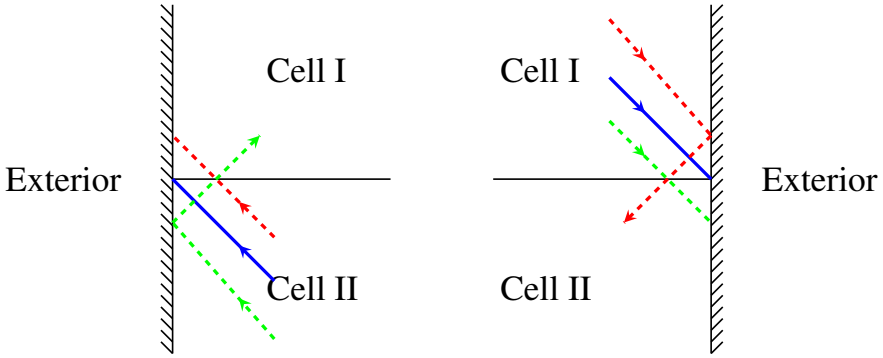

Figure 9. Illustration of Corner Splitting Method For Exterior Cells